

Application of the Hybrid Finite Element Method to Aircraft Repairs

REFERENCE: Tong, P., Greif, R., and Chen, L., "Application of the Hybrid Finite Element Method to Aircraft Repairs," *Fracture Mechanics: Twenty-Second Symposium (Volume II)*, ASTM STP 1131, S. N. Atluri, J. C. Newman, Jr., I. S. Raju, and J. S. Epstein, Eds., American Society for Testing and Materials, Philadelphia, 1992, pp. 154–169.

ABSTRACT: A hybrid finite element approach is presented for the analysis of cracked panels with riveted doublers in airframe structures. The method uses the super element developed by Tong to model the cracked panel with rivet holes, springs to model the rivets, and regular finite elements to model the doubler. The super element accurately models the crack and rivet holes of the skin while the regular finite element method provides the versatility to take into account the variety of doubler designs. Numerical results are presented to demonstrate the efficiency and accuracy of this approach, and to compare different doubler designs.

KEY WORDS: fracture mechanics, fatigue (materials), finite element method, aircraft structures, aircraft repairs

In December 1978, the Federal Aviation Administration of the United States (FAA) issued the Amendment 45 to the FAR 25.571, Fatigue Evaluation of Flight Structure, requiring that the structure of all new transport category airplanes certificated in the United States be designed to damage tolerant principles. This is a requirement [1] that methods of advanced fracture mechanics be applied to evaluating the structural integrity of aircraft to ascertain that the airframe will not experience catastrophic failure due to fatigue, corrosion, or accidental damage under the expected load spectra throughout the operating life of the aircraft. In 1981, the FAA further issued advisory circular AC 91.56 providing guidance for development of the Supplemental Inspection Documents (SIDs) based on the damage tolerant philosophy for existing large transport category airplanes. Since then, aircraft manufacturers have carried out damage tolerant evaluations to define inspection programs for both new designs and the existing older transport category airplanes.

Damage tolerant evaluation is not normally performed for repairs and modifications to principal structural elements. The current practice generally assures that repairs or modifications would have an equal or better static strength as compared to the original design. In Ref 2, Swift shows how these repairs and modifications can degrade the damage tolerance of the structure. The main causes for the degradation are due to the bearing loads and stress concentration induced on the rivet holes at the location of repair and the reduced inspect-

¹Professor and head, Mechanical Engineering Department, Hong Kong University of Science and Technology, Hong Kong. Dr. Tong is currently on leave from the Volpe National Transportation Systems Center, U.S. Department of Transportation, Cambridge, MA 02142.

²Transportation Systems Center, U.S. Department of Transportation, Cambridge, MA 02142; also, Professor of Mechanical Engineering, Tufts University, Medford, MA 02155.

³Graduate student, Department of Mechanical Engineering, Tufts University, Medford, MA 02155.

ability of these holes because they are covered by the doubler. He has suggested a number of approaches to improve the design of these repairs to reduce the rivet forces, improve the inspectability, and consequently increase the fatigue life and damage tolerance of the repaired basic structure.

Swift uses the displacement compatibility method to determine the rivet forces and the bearing stresses in the holes of built-up panels. The present paper presents a hybrid method for the analysis of cracked panels with riveted doublers. The method uses the super-element developed in Ref 3 with a slight modification to model the cracked panel with rivet holes, springs to model the rivets, and regular finite elements to model the doublers. The super-element accurately models the crack and rivet holes of the skin while the regular finite method provides the versatility to take into account the variety of doubler designs.

As mentioned in Ref 3, the standard finite element method is versatile enough to take into account the effects of complex geometry variations, and different stiffener and fastener configurations. However, in order to account for the stress singularities at crack tips and rapid stress variations near rivet holes, enormous amounts of elements are required to model the structure with any degree of accuracy. Thus for an efficient finite element solution, it is natural to employ a hybrid super-element to account for the singular behavior. It is seen from Ref 4, that the use of the hybrid super-element to solve problems for structural components with cracks is extremely accurate and efficient in comparison to the standard finite element method.

Hybrid Formulation

Airframe structures often involve skins with bonded or riveted stiffeners. If the skin is damaged, a doubler(s) is riveted over the damaged area. Loads are transferred out of the skin to the doubler through the rivets. The bearing stress induced in the rivet holes will degrade the fatigue life of the skin. Therefore, it is essential to determine the rivet loads in order to quantify the effects of repairs on the damage tolerance of the structure. The hybrid finite element method is ideal for analysis that can accurately calculate the singular stresses at the crack tips and the nearly singular stresses around the rivet holes.

Following the formulation given in Ref 3, we approximate the skin as an infinite panel with a centrally located crack of length $2a$ (Fig. 1). Remote stresses, σ_{11}^0 , σ_{22}^0 , and σ_{12}^0 , are applied. The panel is also subjected to loads, P^k , along the surfaces of small holes at z_k , $k = 1, 2, \dots$. Complex variables are used in this formulation where

$$z = x + iy$$

$$P^k = X^k + iY^k \quad (1)$$

in which X^k and Y^k denote the load per unit thickness in the x and y directions, respectively. The load at z_k is applied on the hole surface of radius $|z - z_k| = \epsilon$ where ϵ is small as compared to any characteristic dimension (such as the half crack length) of the problem. The applied forces are in self-equilibrium, that is

$$\sum_k P^k = 0 \quad (2)$$

$$\text{Im} \left(\sum_k P^k \bar{z}_k \right) = 0 \quad (3)$$

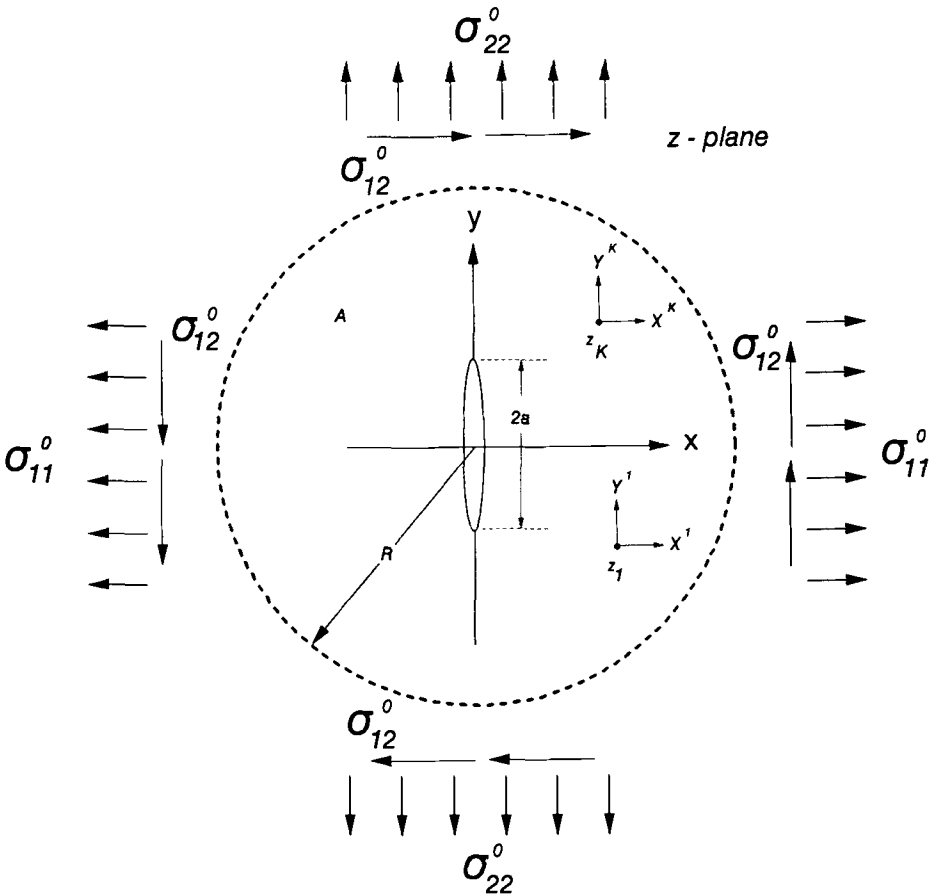


FIG. 1—Concentrated loads and remote stresses on a cracked panel.

Equations 2 and 3 are, respectively, the force and the moment equilibrium equations, and $Im()$ denotes the imaginary part.

A hybrid variational functional for the panel can be written as

$$\begin{aligned} \pi_p = & \sum_k \int_{|z-z_k|=\epsilon} t T_i \bar{u}_i ds - t \left(\int_A U(\sigma_{ij}) dA - \int_A U(\sigma_{ij}^0) dA \right) \\ & + \int_{R \rightarrow \infty} t T_i \bar{u}_i^0 ds - \int_{R \rightarrow \infty} t T_i^0 \bar{u}_i^0 ds \end{aligned} \quad (4)$$

where t is the panel thickness; u_i are the displacements; $T_i (= \sigma_{ij} n_j)$ and σ_{ij} are, respectively, the boundary tractions and stresses; and $U(\sigma_{ij})$ is the complementary energy per unit volume. In Eq 4, we required that σ_{ij} satisfy a priori the equilibrium conditions in A and the traction-free conditions at the crack surface. The superscript, $()^0$, denotes the known quantities associated with the solution of a cracked panel without holes subjected to given remote stresses. Therefore, the second term in the parenthesis and the last term on the right side

are constants that have no effect on the functional variation. The \tilde{u}_i are the displacements of the skin at the hole surface, $|z - z_k| = \varepsilon$, and are independent functional variables of π_p . The Euler equations for the panel can be derived through the first variation of π_p . They are the compatibility equations in A , at the hole surfaces, and at $R(\rightarrow \infty)$.

Let us write

$$\begin{aligned}\sigma_{ij} &= \hat{\sigma}_{ij} + \sigma_{ij}^o \\ T_i &= \hat{T}_i + T_i^o\end{aligned}\quad (5)$$

In addition, we will choose σ_{ij} to satisfy also a priori the compatibility equation in A . In other words, σ_{ij} are selected such that an associated compatible displacement field, u_i , in A exists. Writing u_i in the form

$$u_i = \hat{u}_i + u_i^o \quad (6)$$

substituting both Eqs 5 and 6 into Eq 4, and converting the area integration to line integration, π_p becomes

$$\pi_p = t \left[\sum_k \int_{|z - z_k| = \varepsilon} \left(T_i \tilde{u}_i - \hat{T}_i \hat{u}_i^o - \frac{1}{2} \hat{T}_i \hat{u}_i \right) ds - \frac{1}{2} \int_{R \rightarrow \infty} \hat{T}_i \hat{u}_i dS \right] \quad (7)$$

The detailed derivation of σ_{ij} and u_i are given in Ref 3, which expresses the solution in terms of two stress functions (ϕ, ψ) .

The remote stress solution without holes [5] is

$$\begin{aligned}\phi^o(\zeta) &= \frac{a}{8} \left[\sigma_{22}^o \left(\zeta - \frac{1}{\zeta} \right) + \sigma_{11}^o \left(\zeta + \frac{3}{\zeta} \right) + \frac{4i\sigma_{12}^o}{\zeta} \right] \\ \psi^o(\zeta) &= \frac{a}{4} \left[\sigma_{22}^o \left(\zeta - \frac{1}{\zeta} \right) - \sigma_{11}^o \left(\zeta - \frac{1}{\zeta} + \frac{4\zeta}{1 + \zeta^2} \right) + 2\sigma_{12}^o i \left(\zeta + \frac{1}{\zeta} - \frac{2\zeta}{1 + \zeta^2} \right) \right]\end{aligned}\quad (8)$$

where ζ and z are related by

$$\begin{aligned}z &= \frac{a}{2} \left(\zeta - \frac{1}{\zeta} \right) \\ \zeta &= \frac{z}{a} + \sqrt{1 + \left(\frac{z}{a} \right)^2}\end{aligned}\quad (9)$$

The branch of the square root in Eq 9 is chosen to ensure that $|\zeta| \geq 1$. The transformation in Eq 9 maps the cracks surface in the z -plane to the unit circle centered at the origin in the ζ -plane.

The solution for a panel with a crack and concentrated load, P^k , at ζ^k is [3,6]

$$\begin{aligned} \phi^k(\zeta) = & -\frac{P^k}{2(\kappa + 1)\pi} \ln(\zeta - \zeta_k) - \frac{\kappa P^k}{2(\kappa + 1)\pi} \ln\left(\frac{1}{\zeta} - \bar{\zeta}_k\right) \\ & - \frac{\bar{P}^k}{2(\kappa + 1)\pi} \frac{\bar{\zeta}_k\left(\zeta_k - \frac{1}{\zeta_k} + \bar{\zeta}_k - \frac{1}{\bar{\zeta}_k}\right)}{(1 + \bar{\zeta}_k^2)(1 - \zeta\bar{\zeta}_k)} \\ & - \frac{\bar{P}^k}{2\pi(\kappa + 1)} \frac{4\bar{\zeta}_k^2\epsilon^2}{(1 + \bar{\zeta}_k^2)^2a^2} \frac{1}{(1 - \zeta\bar{\zeta}_k)^2} \\ & + \frac{P^k}{2\pi(\kappa + 1)^2} [\ln(-\zeta_k) + \kappa^2\ln(-\bar{\zeta}_k)] \\ & + \frac{\bar{P}^k}{2\pi(\kappa + 1)^2} \left[\frac{\left(\zeta_k - \frac{1}{\zeta_k}\right)\bar{\zeta}_k - 2}{1 + \bar{\zeta}_k^2} \right] \end{aligned} \quad (10)$$

and

$$\psi(\zeta) = -\bar{\phi}\left(\frac{1}{\zeta}\right) - \frac{\zeta(1 - \zeta^2)}{1 + \zeta^2} \phi'(\zeta) \quad (11)$$

where ϵ is the radius of the hole at ζ_k and

$$\begin{aligned} \kappa &= \frac{3 - \nu}{1 + \nu} \quad \text{for plane stress} \\ &= 3 - 4\nu \quad \text{for plane strain} \end{aligned} \quad (12)$$

in which ν is the Poisson's ratio. The short bar over ϕ denotes the complex conjugate of ϕ , but not the independent variable itself.

For the case that the radii of the rivet holes are sufficiently small, we can approximate the stress functions for σ_{ij} as the sum of the solutions for concentrated loads at ζ_k , that is

$$\begin{aligned} \phi(\zeta) &= \sum_k \phi^k(\zeta) \\ \psi(\zeta) &= \sum_k \psi^k(\zeta) \end{aligned} \quad (13)$$

The expression in Eq 10 is the same as that of Eq 21 of Ref 3 except for the last three terms. The first of these three terms is added to ensure that the $O(1)$ displacements of (u_1, u_2) on the rivet hole surfaces are independent of θ , the local angle defining each rivet hole. The last two terms are constants having no effects on the stress distribution and are added for the convenience of programming so that the **H** flexibility matrix in Eq 24 is symmetric.

Returning to Eq 7, recall that T_i and u_i are the tractions and displacements associated with the equilibrating and compatible stress field, σ_{ij} , which also satisfies the traction-free conditions at the crack surface. The integration over $R \rightarrow \infty$ is zero [3]. If the radii of the holes are sufficiently small, the integration over $|z - z_k| = \epsilon$ can be carried out explicitly.

Because \bar{u}_i and u_i° have no singularity in A , as $\varepsilon \rightarrow 0$, we have

$$\begin{aligned} \int_{|z-z_k|=\varepsilon} T_i \bar{u}_i ds &= X^k(\bar{u})_k + Y^k(\bar{v})_k + 0(\varepsilon^2) \\ \int_{|z-z_k|=\varepsilon} \hat{T}_i u_i^\circ ds &= X^k(u^\circ)_k + Y^k(v^\circ)_k + 0(\varepsilon^2) \end{aligned} \quad (14)$$

where $(\bar{u}, \bar{v})_k$ and $(u^\circ, v^\circ)_k$ are the values of (\bar{u}_1, \bar{u}_2) and (u_1°, u_2°) at z_k , respectively. We have

$$\begin{aligned} 2\mu(u_1^\circ + iu_2^\circ) &= \sigma_{11}^\circ \frac{a}{8} \left[\kappa \left(\zeta + \frac{3}{\bar{\zeta}} \right) - \frac{\left(\zeta - \frac{1}{\bar{\zeta}} \right)}{1 + \bar{\zeta}^2} (\bar{\zeta}^2 - 3) + 2 \left(\bar{\zeta} - \frac{1}{\bar{\zeta}} + \frac{4\bar{\zeta}}{1 + \bar{\zeta}^2} \right) \right]_k \\ &+ \sigma_{22}^\circ \frac{a}{8} \left[(\kappa - 1) \left(\zeta - \frac{1}{\bar{\zeta}} \right) - 2 \left(\bar{\zeta} - \frac{1}{\bar{\zeta}} \right) \right]_k + \sigma_{12}^\circ \frac{ai}{2} \left[\frac{\kappa}{\bar{\zeta}} - \frac{\zeta - \frac{1}{\bar{\zeta}} + \bar{\zeta} - \frac{1}{\bar{\zeta}}}{1 + \bar{\zeta}^2} + \bar{\zeta} \right]_k \end{aligned}$$

The integration of $\hat{T}_i \hat{u}_i$ over $|z - z_j| = \varepsilon$ with $\varepsilon \rightarrow 0$ can be performed easily in polar coordinates in the z -plane, that is

$$\int_{|z-z_j|=\varepsilon} \hat{T}_i \hat{u}_i ds = \operatorname{Re} \int_0^{2\pi} -(\hat{\sigma}_{rr} - i\hat{\sigma}_{r\theta})(\hat{u}_r + i\hat{u}_\theta) \varepsilon d\theta \quad (15)$$

in which Re denotes the real part of a complex function, and

$$\begin{aligned} \hat{u}_r + i\hat{u}_\theta &= e^{-i\theta}(\hat{u}_1 + i\hat{u}_2) = \frac{e^{-i\theta}}{2\mu} \left(\kappa\phi - z \frac{d\bar{\phi}}{dz} - \bar{\psi} \right) \\ \hat{\sigma}_{rr} - i\hat{\sigma}_{r\theta} &= \frac{d\phi}{dz} + \frac{d\bar{\phi}}{dz} - e^{2i\theta} \left(\bar{z} \frac{d^2\phi}{dz^2} + \frac{d\psi}{dz} \right) \end{aligned} \quad (16)$$

where μ is the shear modulus.

Using Eqs 10, 11, and 13, we find

$$\hat{\sigma}_{rr} - i\hat{\sigma}_{r\theta} = -\bar{P} \frac{e^{i\theta}}{2\pi\varepsilon} + 0(1) \quad (17)$$

at $z = z_j + \varepsilon e^{i\theta}$. Similarly, we obtain

$$\hat{u}_r + i\hat{u}_\theta = e^{-i\theta} \sum_{j \neq i} \{P^k[d^k(\zeta_j) + f^k(\zeta_j)] + \bar{P}^k[e^k(\zeta_j) + g^k(\zeta_j)]\} + 0(\varepsilon) \quad (18)$$

The functions $d^k(\zeta)$, $e^k(\zeta)$, $f^k(\zeta)$, and $g^k(\zeta)$ are defined as follows. For $\zeta \neq \zeta_k$,

$$f^k(\zeta) = \frac{1}{4(\kappa + 1)\mu\pi} \left[-\ln\left(1 - \frac{1}{\zeta_k \bar{\zeta}}\right) - \kappa^2 \ln\left(1 - \frac{1}{\bar{\zeta}_k \zeta}\right) \right. \\ \left. + \frac{\left(\zeta - \frac{1}{\zeta} + \bar{\zeta} - \frac{1}{\bar{\zeta}}\right) \left(\zeta_k - \frac{1}{\zeta_k} + \bar{\zeta}_k - \frac{1}{\bar{\zeta}_k}\right) \bar{\zeta}^2 \zeta_k^2}{(1 + \bar{\zeta}^2)(1 + \zeta_k^2)(1 - \bar{\zeta} \zeta_k)^2} \right] \quad (19)$$

$$g^k(\zeta) = \frac{1}{4(\kappa + 1)\mu\pi} \left[\frac{2(\bar{\zeta} \bar{\zeta}_k - 1)}{(1 + \bar{\zeta}^2)(1 + \bar{\zeta}_k^2)} - \frac{\kappa \bar{\zeta}_k \left(\zeta_k - \frac{1}{\zeta_k} + \bar{\zeta}_k - \frac{1}{\bar{\zeta}_k}\right)}{(1 + \bar{\zeta}_k^2)(1 - \bar{\zeta} \zeta_k)} \right. \\ \left. - \frac{\kappa \bar{\zeta} \left(\zeta - \frac{1}{\zeta} + \bar{\zeta} - \frac{1}{\bar{\zeta}}\right)}{(1 + \bar{\zeta}^2)(1 - \bar{\zeta} \zeta_k)} \right]$$

$$d^k(\zeta) = -\frac{\kappa}{4(\kappa + 1)\mu\pi} \ln(\zeta - \zeta_k)(\bar{\zeta} - \bar{\zeta}_k)$$

$$e^k(\zeta) = \frac{1}{4(\kappa + 1)\mu\pi} \left[\frac{\left(\zeta - \frac{1}{\zeta}\right) \bar{\zeta}^2}{1 + \bar{\zeta}^2} - \frac{\left(\zeta_k - \frac{1}{\zeta_k}\right) \bar{\zeta}_k^2}{1 + \bar{\zeta}_k^2} \right] \frac{1}{\bar{\zeta} - \bar{\zeta}_k} \quad (20)$$

and if $\zeta \equiv \zeta_k$

$$d^k(\zeta_k) = -\frac{\kappa}{4(\kappa + 1)\mu\pi} \ln \left[\frac{4\epsilon^2 \bar{\zeta}_k^2 \zeta_k^2}{a^2(1 + \bar{\zeta}_k^2)(1 + \zeta_k^2)} \right] \quad (21)$$

$$e^k(\zeta_k) = \frac{1}{4(\kappa + 1)\mu\pi} \frac{2\left(\zeta_k - \frac{1}{\zeta_k}\right) \bar{\zeta}_k}{(1 + \bar{\zeta}_k^2)^2}$$

The functions d , e , f , and g are each different from those of Eqs 28 through 30 of Ref 3 by a constant that has no effect for the stress distribution.

A substitution of Eqs 17 through 21 into Eq 15 yields

$$\int_{|z - z_j| = \epsilon} \hat{T}_i \hat{u}_i ds = Re \left[\bar{P}^j \sum_k (P^k D_j^k + \bar{P}^k E_j^k) \right] + 0(\epsilon^2) \quad (22)$$

where

$$D_j^k = d^k(\zeta_j) + f^k(\zeta_j) \quad (23)$$

$$E_j^k = e^k(\zeta_j) + g^k(\zeta_j)$$

It is noted that the integration of 0(1) terms in the integrand is zero. After some algebraic manipulations, we get

$$\sum_j \int_{|z-z_j|=\epsilon} \hat{T}_i \hat{u}_i ds = (\mathbf{X}^T \mathbf{Y}^T) \begin{pmatrix} \mathbf{H}_{1R} & \text{sym} \\ \mathbf{H}_{1I} & \mathbf{H}_{2R} \end{pmatrix} \begin{pmatrix} \mathbf{X} \\ \mathbf{Y} \end{pmatrix} \quad (24)$$

where $(\)^T$ denotes the transpose, the subscripts $(\)_R$ and $(\)_I$ respectively denote the real and imaginary parts, $(\)$ denotes a vector or a matrix, and

$$\begin{aligned} \mathbf{X}^T &= (X^1, X^2, \dots) \\ \mathbf{Y}^T &= (Y^1, Y^2, \dots) \\ \mathbf{H}_1 &= [D_j^k + E_j^k] \\ \mathbf{H}_2 &= [D_j^k - E_j^k] \end{aligned} \quad (25)$$

It is noted that

$$\begin{aligned} \mathbf{H}_{1R} &= \mathbf{H}_{1R}^T \\ \mathbf{H}_{2R} &= \mathbf{H}_{2R}^T \\ \mathbf{H}_{1I} &= -\mathbf{H}_{2I}^T \end{aligned} \quad (26)$$

so that the flexibility matrix \mathbf{H} of Eq 24 is symmetric.

Hybrid Functional for Repaired Panel

The repaired panel shown in Fig. 2 consists of three parts: the skin, rivets, and a doubler.⁴ The variational functional of the panel is simply the sum of the functional of the three components. Each of the rivets is modeled as a series of springs representing the flexibility of the rivet stem and the adjacent holes of the skin and doubler. The stiffness of each spring element is shown in Fig. 3a, where E_s , E_r , and E_d are, respectively, the Young's moduli of the skin, rivet, and doubler; D is the rivet diameter; and t and t_d are the thickness of the panel and the doubler, respectively. The constants A_1 and A_2 are obtained empirically through tests [2] and are, respectively, 5 and 0.8 for aluminum rivets, and 1.666 and 0.86 for steel fasteners. The compliance coefficient of the rivet is

$$\alpha = \left(\frac{A_1}{E_r D} + \frac{A_2}{E_s t} + \frac{A_2}{E_d t_d} \right) \quad (27)$$

Using the complementary energy formulation [3], the variational functional for the rivets can be written as

$$\pi_r = \sum_k \left[(u_d - \bar{u})_k F_x^k + (v_d - \bar{v})_k F_y^k - \frac{1}{2} \alpha [(F_x^k)^2 + (F_y^k)^2] \right] \quad (28)$$

⁴The original data used non-SI units.

where \mathbf{e} is the strain vector, \mathbf{C} is the elastic coefficient matrix per unit thickness, and A is the area of the doubler.

Using Eqs 7, 28, and 29, we have the functional for the repaired panel

$$\pi = \pi_p + \pi_d + \pi_r \quad (30)$$

which can be used to derive the finite element equations. The number of unknowns of the finite element equations can be reduced by eliminating the rivet displacements at the skin $(\bar{u}, \bar{v})_k$, and the rivet forces, (F_x^k, F_y^k) . We shall consider the following two doubler designs.

(a) *Single Doubler (Fig. 2)*

The first variation of π with respect to (F_x^k, F_y^k) and $(\bar{u}, \bar{v})_k$ gives

$$\begin{aligned} \alpha F_x^k &= (u_d)_k - (\bar{u})_k \\ \alpha F_y^k &= (v_d)_k - (\bar{v})_k \end{aligned} \quad (31)$$

and

$$\begin{aligned} F_x^k &= tX^k \\ F_y^k &= tY^k \end{aligned} \quad (32)$$

Requiring that the relationships between (F_x^k, F_y^k) and (X^k, Y^k) are satisfied a priori, Eq 30 reduces to

$$\begin{aligned} \pi &= - \sum_k t \left[X^k (u^o)_k + Y^k (v^o)_k + \int_{|z-z_k|=\epsilon} \frac{1}{2} \hat{T}_i \hat{u}_i ds \right] \\ &+ \sum_k t \left\{ X^k (u_d)_k + Y^k (v_d)_k - \frac{1}{2} \alpha t [(X^k)^2 + (Y^k)^2] \right\} + \pi_d \end{aligned} \quad (33)$$

The independent field variables for Eq 33 are the doubler deflections $(u_d, v_d)_k$ and the stress functions (ϕ, ψ) with the nodal values of the deflection and rivet loads (X^k, Y^k) , respectively, being the unknowns for the finite-element equations.

(b) *Doubler Lamination: Two-Side Doublers (Fig. 4)*

This is a design that can be used to reduce the abrupt change of bending rigidity at the edge of the doubler and, hence, minimize the induced bending stresses on the skin. This design also reduces the forces of the rivets of the first row to improve the life of the skin. For this design, we can model the flexibility around the holes of the doublers as two parallel springs (Fig. 3b). The variational functional for the rivets can be written as

$$\begin{aligned} \pi_r &= \frac{1}{2} \sum_k [K(\bar{u} - \bar{u})^2 + K(\bar{v} - \bar{v})^2 + K_{ds}(u_{ds} - \bar{u})^2 \\ &+ K_{ds}(v_{ds} - \bar{v})^2 + K_{dp}(u_{dp} - \bar{u})^2 + K_{dp}(v_{dp} - \bar{v})^2]_k \end{aligned} \quad (34)$$

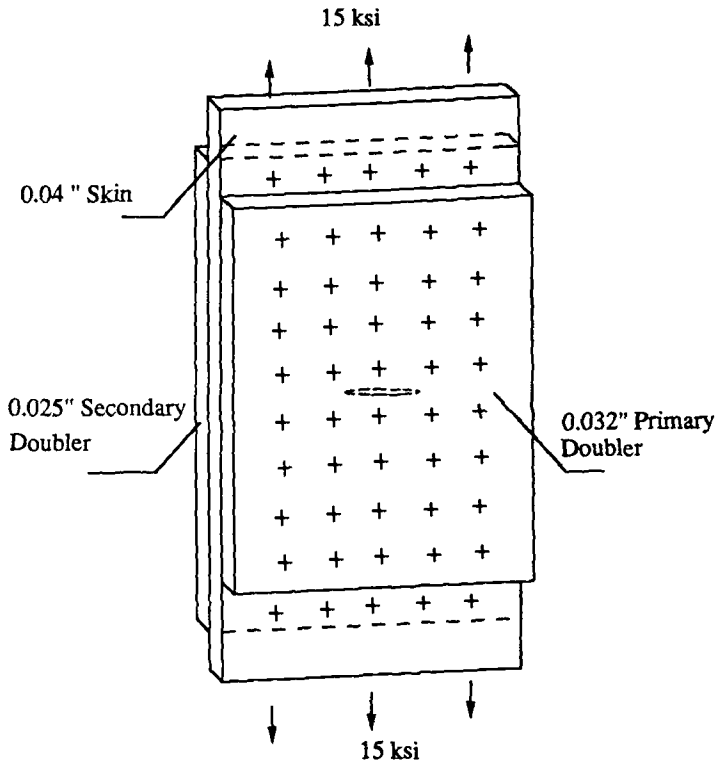


FIG. 4—Two-side doubler lamination.

where $(\bar{u}, \bar{v})_k$ are the fictitious displacements between the springs representing the rivet stem and the doubler holes and

$$\begin{aligned} \frac{1}{K} &= \frac{A_2}{E_s t} + \frac{A_1}{E_r D} \quad (\text{rivet stem and skin in series}) \\ K_{ds} &= \frac{E_d t_{ds}}{A_2} \\ K_{dp} &= \frac{E_d t_{dp}}{A_2} \end{aligned} \tag{35}$$

are stiffnesses of the spring elements with the subscripts, s and p , denoting quantities associated with the secondary and primary doublers.

The functional for the doublers is in the same form as that in Eq 29 except that the domain of integration now includes the area of both doublers. The first variation of π with respect to the displacements $(\bar{u}, \bar{v})_k$, and $(\bar{u}, \bar{v})_k$ gives

$$\begin{aligned} tX &= K(\bar{u} - \bar{u}) \\ tY &= K(\bar{v} - \bar{v}) \end{aligned} \tag{36}$$

$$\begin{aligned} K(\bar{u} - \bar{u}) + K_{ds}(\bar{u} - u_{ds}) + K_{dp}(\bar{u} - u_{dp}) &= 0 \\ K(\bar{v} - \bar{v}) + K_{ds}(\bar{v} - v_{ds}) + K_{dp}(\bar{v} - v_{dp}) &= 0 \end{aligned} \quad (37)$$

In Eqs 36 and 37 and in the subsequent discussion, the subscripts and superscripts, k , are dropped for convenience. We can solve for (\bar{u}, \bar{v}) and (\bar{u}, \bar{v}) in terms of (X, Y) , (u_{ds}, v_{ds}) , and (u_{dp}, v_{dp}) . Eliminating (\bar{u}, \bar{v}) and (\bar{u}, \bar{v}) , the functional, π , then becomes

$$\begin{aligned} \pi &= \pi_d - \sum_k t \left[X^k (u^o)_k + Y^k (v^o)_k + \int_{|z-z_k|=\epsilon} \frac{1}{2} \hat{T}_i \hat{u}_i ds \right] \\ &+ \frac{1}{2} \sum_k \left\{ (X, u_{ds}, u_{dp}) \mathbf{K} \begin{pmatrix} X \\ u_{ds} \\ u_{dp} \end{pmatrix} + (Y, v_{ds}, v_{dp}) \mathbf{K} \begin{pmatrix} Y \\ v_{ds} \\ v_{dp} \end{pmatrix} \right\}_k \end{aligned} \quad (38)$$

where \mathbf{K} is given by the matrix

$$\mathbf{K} = \begin{pmatrix} -t^2 \left(\frac{1}{K} + \frac{1}{K_{ds} + K_{dp}} \right) & \text{sym} \\ \frac{tK_{ds}}{K_{ds} + K_{dp}} & \frac{K_{ds}K_{dp}}{K_{ds} + K_{dp}} \\ \frac{tK_{dp}}{K_{ds} + K_{dp}} & \frac{-K_{ds}K_{dp}}{K_{ds} + K_{dp}} \quad \frac{K_{ds}K_{dp}}{K_{ds} + K_{dp}} \end{pmatrix} \quad (39)$$

The independent variables for the functional are the doubler deflections $(u_{dm}, v_{dm})_k$ where $m = s$ and p , and the loads (X^k, Y^k) , the rivet loads on the panel per unit thickness. The nodal values of these quantities are the unknowns for the finite-element equations.

Examples

Figure 5 shows the results for a fuselage skin of thickness 1 mm (0.04 in.) with a crack of length $2a$. A doubler of thickness 1.27 mm (0.05 in.) is riveted over the damaged area with four rows of rivets on each side of the crack in the x direction. Each row contains 25 rivets, running from $y = -304.8$ mm (-12 in.) to $y = +304.8$ mm ($+12$ in.). The rivet diameter is 4.76 mm ($3/16$ in.) and the rivet pitch is 25.4 mm (1 in.). The results for rivet forces, F_x , are shown in Fig. 5 for the case that the skin, rivets, and doublers are all made of aluminum ($E = 10^7$ psi, $\nu = 0.33$) with a crack length of $2a = 50.8$ mm (2 in.). It is seen that the higher rivet loads are at the first row of rivets ($x = +88.9$ mm) ($+3.5$ in.) that connects the doubler to the skin, with the highest force of 103 kg (227 lb) at the corner rivet ($x = 3.5$ in., $y = 12$ in.) where both edges of the doubler come together.

As a comparison to these rivet loads, the results of Swift [2] that are based on the displacement compatibility method are also shown. Although the rivet loads from Ref 2 are based on a skin without a crack, the present finite element results for a small crack, $a = 1$ in., are an adequate comparison. The maximum rivet load, F_x , from Ref 2 is 85 kg (187 lb), which is 18% less than the present result of 103 kg (227 lb). This difference is mainly due to the inclusion of two-dimensional effects in the present finite element analysis, in comparison to the one-dimensional effects of the displacement compatibility method. Since the finite element results accurately model the effects at the first row of the doubler/skin

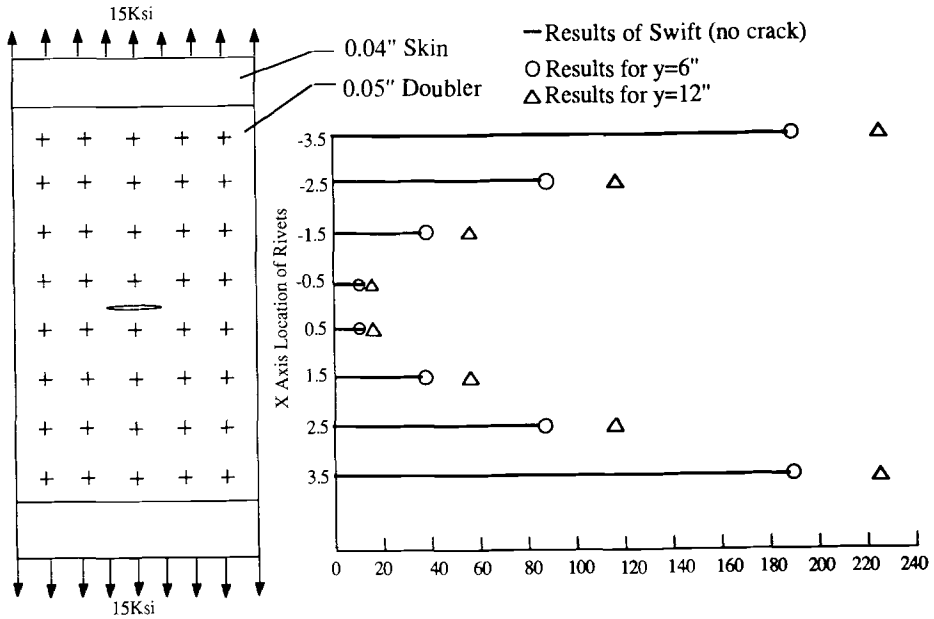


FIG. 5—Rivet load distribution (lb), F_x , single doubler, crack length $2a = 2$ in. (50.8 mm).

intersection, it is physically most plausible to compare with Ref 2 halfway along this edge row of rivets at $y = 152.4$ mm (6 in.), which minimizes the effects of both the crack and the corner effect where the edges of the doubler come together. At this location, the present finite element technique produces a rivet load of 85.4 kg (188 lb). As seen in Fig. 5, the comparison of rivet loads at $y = 152.4$ mm (6 in.) shows excellent agreement. Another factor of importance is the effect of rivet load in the y direction, that is, normal to direction of applied stress of 103.4 MPa (15 ksi). For the maximum rivet load of $F_{x,max} = 103$ kg (227 lb), there is also a load component in y direction of 34.5 kg (76 lb), so that the resultant rivet load is actually 108.5 kg (239 lb).

The effect of crack length on the maximum rivet load, F_x , for the corner rivet, $x = 88.9$ mm (3.5 in.), $y = 304.8$ mm (12 in.), is shown in Fig. 6. For a doubler thickness of 1.27 mm (0.05 in.), F_x reaches 134.4 kg (296 lb) when the crack length $2a$ is 609.6 mm (24 in.), that is, the crack reaches all the way to the edge of the doubler. The additional rivet force in the y direction is small and has little effect on the resultant rivet load.

An important indicator of fatigue life is the skin peak bearing stress that is calculated from the maximum rivet force at the corner rivet

$$\sigma_{br} = \frac{F_{max}}{tD} \quad (40)$$

where t is the skin thickness and D is the rivet diameter. For the crack length of 50.8 mm (2 in.), the peak bearing stress is calculated as $\sigma_{br} = 239/(0.04)(0.1875) = 219.7$ MPa (31 867 psi), while for a crack length of 609.6 mm (24 in.) the bearing stress is 272.4 MPa (39 500 psi). The ratio of bearing stress to the gross stress of 103.4 MPa (15 000 psi) is then 2.12 and 2.63 respectively, for 50.8 and 609.6 mm (2 and 24 in.) crack lengths. If the skin is made of 2024-T3, the fatigue life of the basic structure with open holes and a stress ratio

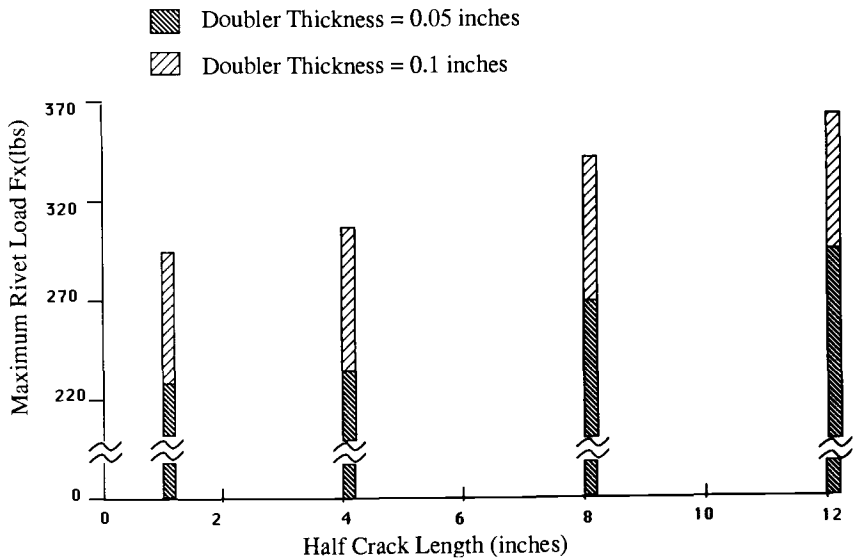


FIG. 6—Maximum rivet load F_x for different crack lengths, single doubler.

of $R = 0$ is 160 000 cycles, but this fatigue life is reduced with increasing ratio of bearing stress to gross stress [2]. With the 1.27 mm (0.05 in.) doubler, the fatigue life is reduced to about 39 000 cycles and 30 000 cycles, respectively, for 50.8 and 609.6 mm (2 and 24 in.) crack lengths, based upon open hole S - n data of Ref 2.

As the thickness of the doubler increases, the rivets in the first (edge) row carry an increasing portion of the load transferred to the doubler. In Fig. 6, the maximum rivet load, F_x , for the corner rivet is plotted as a function of crack length, for a doubler thickness of 2.54 mm (0.10 in.), as well as for 1.27 mm (0.05 in.). The increase in rivet load with crack length, from $a = 25.4$ mm (1 in.) to $a = 304.8$ mm (12 in.), is 17 and 30%, respectively, for a doubler thickness of 2.54 and 1.27 mm (0.10 and 0.05 in.). For a crack length of 609.6 mm (24 in.), the maximum corner rivet force for a 2.54 mm (0.10 in.) doubler is 166.2 kg (366 lb), which is 24% higher than the 134.4 kg (296 lb) force for the 1.27 mm (0.05 in.) doubler. Consequently, the fatigue life of the skin is reduced further by the thicker doubler, even though a thicker doubler can be stronger statically. The effect of doubler thickness on maximum rivet load (corner rivet) is shown in Fig. 7 for 1 mm (0.040 in.) rivet skin thickness. It is seen that the rivet load is affected strongly by the doubler thickness in the range from 1 to 2.5 mm (0.04 to 0.10 in.), rising 45% in this range, which is similar to the result of Swift [2].

A doubler design configuration that can be used to reduce fastener loads in the first doubler row is the use of a multiple doubler as shown in Fig. 4. Placing a secondary doubler on the inside of the panel and extending it one fastener row so that the outer rivet row of the skin only has a single doubler connection, produces a significant advantage in terms of load transfer and inspectability. Consider the case with a 0.63 mm (0.025 in.) inner (secondary) doubler and a 0.81 mm (0.032 in.) outer (primary) doubler. For this configuration and a crack length of $2a = 50.8$ mm (2 in.), the corner rivet load, F_x , $x = 114$ mm (4.5 in.), $y = 304.8$ mm (12 in.), is reduced 22% to 79.9 kg (176 lb) as compared to 103 kg (227 lb), $x = 88.9$ mm (3.5 in.), $y = 304.8$ mm (12 in.), for the 1.27 mm (0.05 in.) single doubler shown in Fig. 5. The skin bearing stress is reduced to 162 MPa (23 466 psi) and the ratio

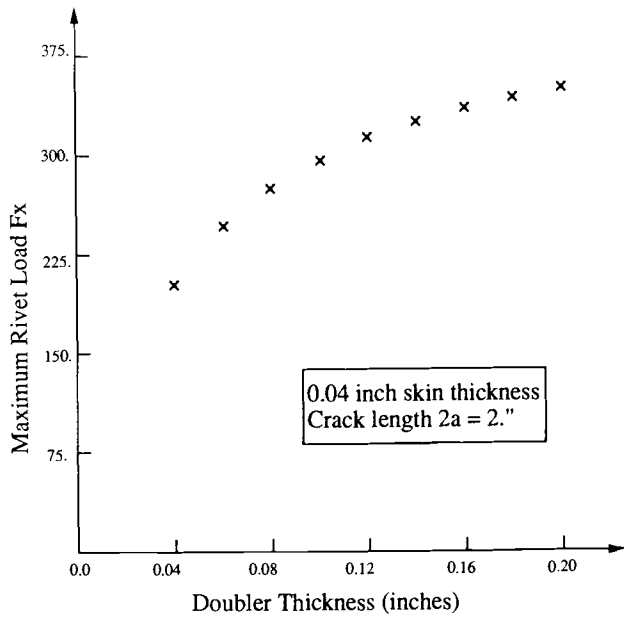


FIG. 7—Effect of doubler thickness on maximum rivet load (corner rivet), single doubler.

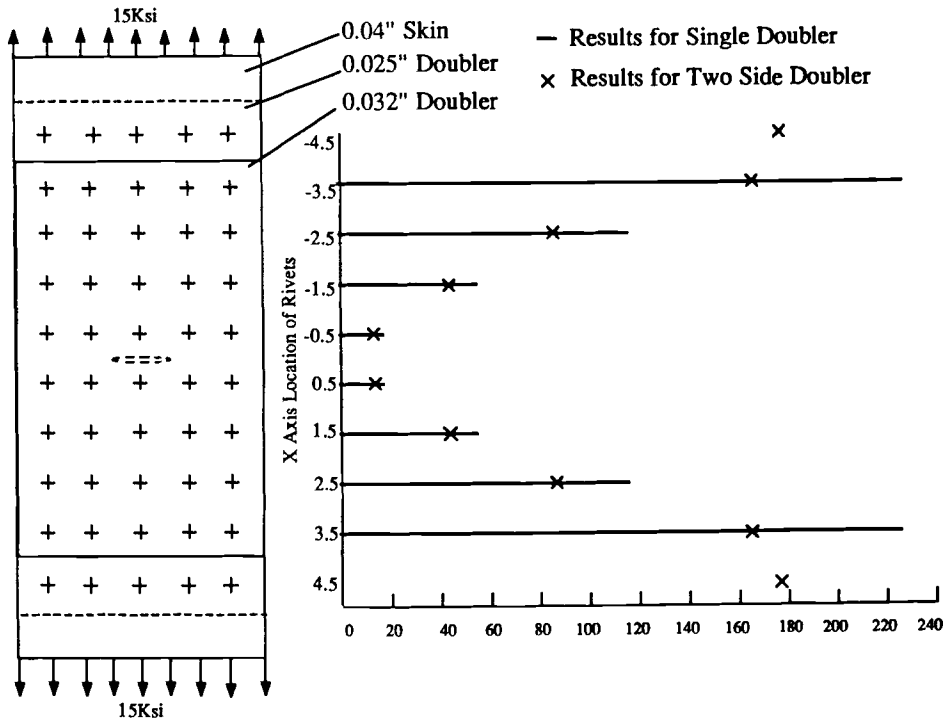


FIG. 8—Rivet load distribution (lb , F_x , two-side doubler, crack length $2a = 2$ in. (50.8 mm).

of bearing stress to gross stress is 1.56, producing an enhanced fatigue life of 55 000 cycles. Additionally, inspectability of this type of doubler repair is improved since a crack in the first rivet row will now be visible. In Ref 2, the critical rivet load, without a crack, is calculated as 55 kg (122 lb), which should be compared to the present rivet load of 66 kg (146 lb) located halfway along the edge row of rivets at $y = 152.4$ mm (6 in.). The difference in this result is due to alternate modeling of the rivet compliance in Ref 2 and the present analysis. The row-by-row rivet load distribution for this two-sided doubler configuration is shown in Fig. 8 for a crack length of 50.8 mm (2 in.).

Acknowledgment

This work was supported by the Federal Aviation Administration Technical Center.

References

- [1] Swift, T., "Damage Tolerance Analysis of Redundant Structures," AGARD Lecture Series No. 97, Fracture Mechanics Design Methodology, Advisory Group for Aerospace Research and Development, Jan. 1979.
- [2] Swift, T., "Repairs to Damage Tolerant Structures," Structural Integrity of Aging Airplanes, S. N. Atluri, Sampath, and P. Tong, Eds., Springer Series in Computational Mechanics, Springer-Verlag, New York, 1991, pp. 433-489.
- [3] Tong, P., "A Hybrid Finite Element Method for Damage Tolerance Analysis," *Computers and Structures*, Vol. 19, No. 1-2, 1984, pp. 263-269.
- [4] Tong, P., Pian, T. H. H., and Lasry, S., "A Hybrid Finite Element Approach to Crack Problems in Plane Elasticity," *International Journal for Numerical Methods in Engineering*, Vol. 7, 1973, pp. 297-308.
- [5] Muskhelishvili, N. I., *Some Basic Problems of Mathematical Theory of Elasticity*, P. Noordhoff, Leyden, The Netherlands, 1953.
- [6] Greif, R., "The Plane Stress Solution of a Concentrated Load in the Presence of a Crack," private communication.